Multiresonant Grating to Replace Transparent Conductive Oxide Electrode for Bias Selected Filtering of Infrared Photoresponse

Tung Huu Dang, Mariarosa Cavallo, Adrien Khalili, Corentin Dabard, Erwan Bossavit, Huichen Zhang, Nicolas Ledos, Yoann Prado, Xavier Lafosse, Claire Abadie, et al.

Multiresonant Grating to replace Transparent Conductive Oxide Electrode for bias selected filtering of infrared photoresponse

Tung Huu Dang[1,2], Mariarosa Cavallo[1], Adrien Khalili[1], Corentin Dabard[1], Erwan Bossavit[1], Huichen Zhang[1], Nicolas Ledos[1], Yoann Prado[1], Xavier Lafosse[3], Claire Abadie[1], Djamal Gacemi[2], Sandrine Ithurria[4], Grégory Vincent[5], Yanko Todorov[2], Carlo Sirtori[2], Angela Vasanelli[2*], Emmanuel Lhuillier[1*]

[1] Sorbonne Université, CNRS, Institut des NanoSciences de Paris, 4 place Jussieu, 75005 Paris, France.
[2] Laboratoire de physique de l'Ecole Normale Supérieure, ENS, Université PSL, CNRS, Sorbonne Université, Université Paris Cité, 24 Rue Lhomond, 75005 Paris, France
[3]Centre de Nanosciences et de Nanotechnologies, CNRS, Univ. Paris-Sud, Université Paris-Saclay, 10 Boulevard Thomas Gobert, 91120 Palaiseau, France
[4] Laboratoire de Physique et d'Etude des Matériaux, ESPCI, PSL Research University, Sorbonne Université, CNRS UMR 8213, 10 rue Vauquelin, 75005 Paris, France.
[5] DOTA, ONERA, Université Paris Saclay, 6 Chem. de la Vauve aux Granges, 91120 Palaiseau, France.

Abstract: Optoelectronic devices rely on conductive layers as electrodes, but they usually introduce optical losses that are detrimental for the device performances. While the use of transparent conductive oxides is established in the visible, these materials show high losses at longer wavelengths. Here, we demonstrate a photodiode based on metallic grating acting as an electrode. The grating generates a multi-resonant photonic structure over the diode stack and allows strong broadband absorption. The obtained device achieves the highest performances reported so far for a mid-wave infrared nanocrystal-based detector, with external quantum efficiency above 90 %, detectivity of 7×10^{11} jones at 80 K at 5 µm, and sub 100 ns time response. Furthermore, we demonstrate that combining different gratings with a single diode stack can generate bias reconfigurable response and develop new functionalities such as band rejection.

Keywords: light-matter coupling, active photonics, reconfigurable response, infrared, nanocrystals, photoresponse.

*To whom correspondence should be sent: angela.vasanelli@ens.fr, el@insp.upmc.fr

Optoelectronic devices rely on semi-transparent electrodes that allow light to be absorbed or emitted from the optically active materials. In the visible range, transparent conductive oxides (TCO), such as ITO (tin-doped indium oxide), AZO (aluminum-doped zinc oxide), or FTO (fluorine-doped tin oxide), play this role by combining a high transmission all over the visible range with high conductivity. When infrared wavelengths are targeted,[1,2] the transmission of the TCO becomes a major concern. In the near-infrared, a trade-off between good conductivity and low optical losses can easily be found by lowering the electrode thickness or carefully tuning the TCO properties.[3] However, both methods come at the price of reduced conductivity and, thus, an increased contact resistance for the device. This may prevent the injection of large currents in light-emitting diodes (LED)[4,5] or result in poor impedance matching for detectors, preventing the fastest device operation. The problem becomes even more dramatic in the mid-wave infrared (MWIR) with low TCO and substrate transmission. In the context of mid-infrared nanocrystal (NC)-based sensing,[6–8] the issue has mostly been swept under the rug. Indeed, until recently, developing diode stacks has been the focus of most of the effort, leaving optical loss in the contacts as a second-order concern. However, the performances of the mid-wave infrared diodes have been significantly improved[9] over the recent years[10] with reported near-unity efficiency, with electroluminescence matching the photoluminescence efficiency in LED,[4] or even for detection. Future improvement will require addressing the problem of contact absorption in the infrared.[11]

Beyond reducing the TCO layer thickness, the most basic strategy to design a partly transparent electrode is to use a metallic grid.[12–16] In this case, the electrode transmission is mainly set by the metal filling factor. On the one hand, the filling factor has to be low to render the electrode transmission as high as possible. On the other hand, a low filling factor not only presents a higher sheet resistance but also lengthens the collection pathways of the photogenerated charges, which is strongly detrimental in the case of low-mobility materials such as NCs. A combination of a metallic grid/pad and thin TCO layer[17,18] has also been tested as an approach to combine transparency and conductivity or as a way to tune the work function of the TCO layer.[19] However, the problem has not been adequately solved. Meanwhile, the Ebessen's group[20] has brought evidence that under certain conditions of resonance, the transmission of a subwavelength aperture can significantly exceed the value set by its filling factor. This pioneer work has later been expanded toward the field of extraordinary optical transmission[21–23] and plasmonic nanohole array.[24,25] Here, we explore the design of a resonant metallic grid[26–28] offering an alternative to TCO as a transparent electrode in the infrared. The grating is designed so that multiple resonances arise, hence allowing a broadband enhancement of the infrared NC absorption. Furthermore, we carefully optimize the geometrical parameters of the diode to maximize the absorption beyond the simple filling factor of the metallic grid. We demonstrate that, by doing so, we are able to obtain the highest performing mid-wave infrared NC-based photodiode reported so far with responsivity close to 3 $A.W^{-1}$, detectivity reaching $7x10^{11}$ jones at 80 K, and a sub-100 ns time response.

In the second part of the paper, we demonstrate the use of these gratings as a strategy to achieve bias reconfigurable photoresponse. So far, the concept of multicolor detectors has been explored independently of bias reconfigurability.[29–31] Bi[32–34] and multicolor[35] response is mainly obtained by associating devices presenting different band edge energies. In particular, bicolor detectors have been obtained by stacking two diodes[33,36] on top of each other, similar to what is done for multi-junction solar cells. However, colloidal fabrication with a large number of steps can be highly challenging. Here, we show that dual-band reconfigurable response can be obtained from a single diode stack. By multiplexing back-to-back diodes with different gratings on a single chip, various operating modes can be obtained, enabling band selection and new functionalities such as narrow-band rejection, which so far remains unreported for nanocrystal-based devices.

Current best mid-wave infrared NC-based diodes rely on the HgTe/Ag_2Te stack, introduced by Ackerman *et al*.[37] In such diodes (**Figure 1**b), the mid-wave infrared absorption relies on HgTe NCs. Here we grow them using the procedure developed by Keuleyan *et al*.[38] The final targeted cut-off

wavelength is 5 µm (*i.e.,* 2000 cm^{-1}), with the grown particles displaying an exciton peak at around 3 µm, as shown in **Figure 1**a. The cut-off wavelength will later be redshifted upon ligand exchange procedure and cooling (see Figure S1 and S14). Initial long-capping ligands are replaced by a mixture of $HgCl_2$ and mercaptoethanol[39,40] to achieve a stronger interparticle coupling as well as to maintain good surface passivation.[41] HgTe with such band edge tends to have an ambipolar character, and Hg or chalcogenides excess on the surface can induce either stronger *n* or p-type behavior.[10] The absorbing layer was initially surrounded by a sapphire substrate, and a thin ITO layer was used as an electron extractor. Sapphire was used instead of glass because the latter has a large absorption above 4 µm, whereas sapphire maintains a high transmission up to 6 µm while remaining cost-effective. The ITO thickness (50 nm, Figure S3) was reduced compared to the typical one used in the visible (180 nm range). At cryogenic temperature (80 K), the stack indeed behaves as a diode presenting a strongly rectifying behavior for the IV curve, see **Figure 1**c and Figure S7 for further characterization. The successful character of this diode has been confirmed by its reuse within the following papers of the same group,[33,42] but also by others,[9,43,44] and can be considered the most efficient platform for NC-based mid-IR sensing to date.

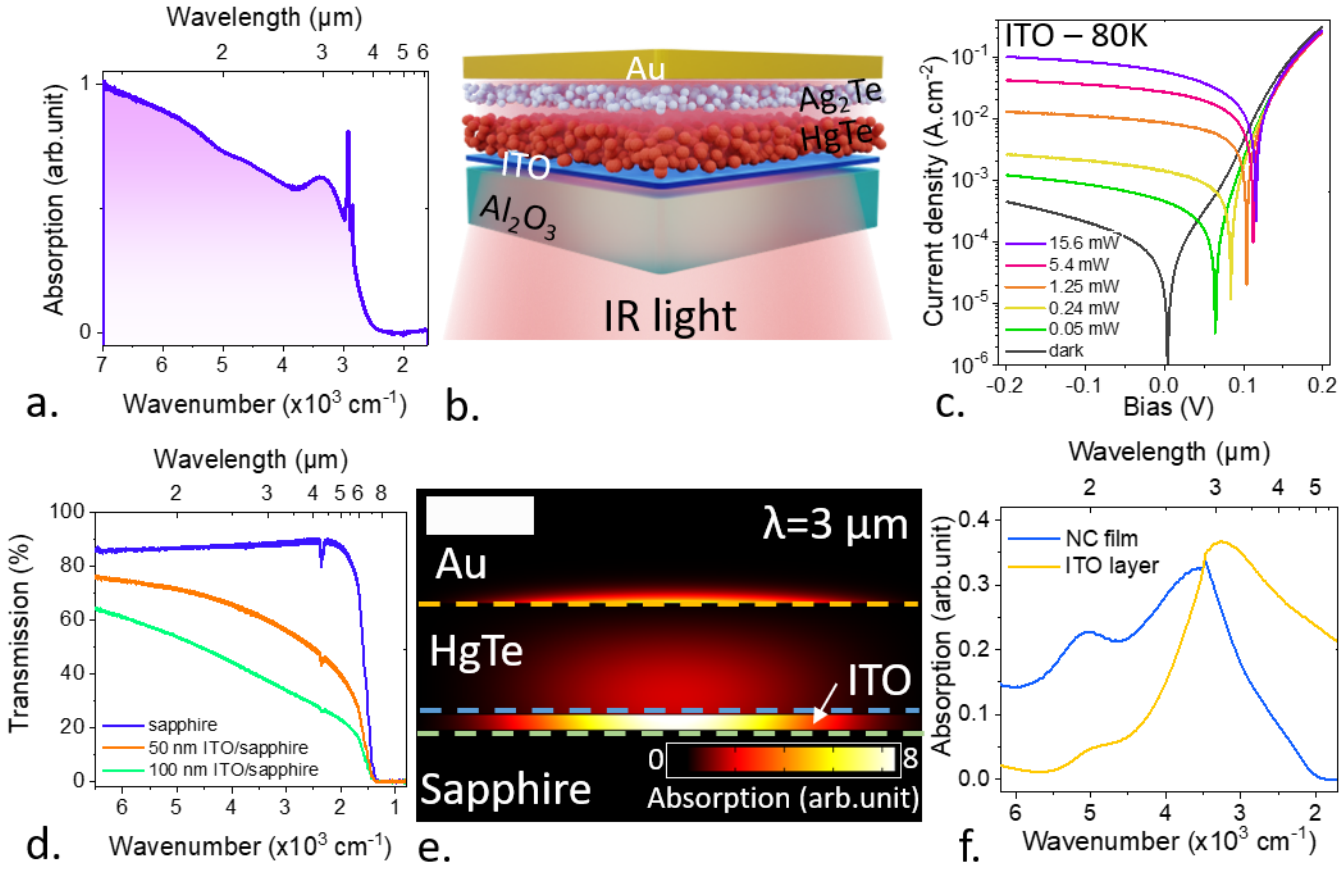

Figure 1 HgTe NC-based photodiode using a transparent conductive oxide as the electrode*. a. Absorption spectrum of HgTe NCs used as MWIR absorber, as they are by the end of synthesis and at room temperature. b. Schematic of a photodiode based on sapphire/ITO/HgTe/Ag_2Te/Au stack. c. I-V curves under dark condition and under illumination (λ ≈ 4.4 µm – the power in the caption is the nominal laser power) measured at 80 K for a diode stack such as the one depicted in b. d. Transmission spectra for a pristine sapphire substrate and for a substrate coated with ITO layer. e. Absorption map (at 3 µm) for the diode stack depicted in b. The scale bar is 350 nm long. f. Simulated absorption spectra within the NC and the ITO for the diode stack depicted in e.*

In spite of this success, the use of ITO remains a clear issue, see **Figure 1**d-f. The transmission of 50 nm ITO at 5 µm is around 40 %. As a result, the targeted device absorption in the range of 3-5

µm (*i.e.,* the atmospheric transparency window that enables long-distance imaging) is not dominated by HgTe but rather by the ITO layer (**Figure 1**e-f), which ends up generating thermal losses rather than photocurrent. In the next part of this paper, we demonstrate that the careful design of a metallic grating offers an interesting alternative to ITO that not only reduces the optical loss in the metal but also shapes the spectral response. Our metallic structure is depicted in **Figure 2**a, S2-4, in which a 1D gold grating replaces the ITO layer. The diode stack remains unchanged (*i.e.,* same material, same order), and only the geometrical parameters will be optimized. The grating size and periodicity are tuned to generate 3 resonances[30]. On top of the gold stripes, metal-dielectric-metal cavities are formed with a first resonance driven by the stripe width through the relation $\lambda=2.n_{eff}.s$, where λ is the resonant wavelength, n_{eff} is the effective modal index, and s is the grating stripe width. This resonance is called TM cavity mode and results from the coupling of the incoming light to the TM_0 mode of the microcavities.[45] We found that s=350 nm induces a resonance at 4.1 µm in TM polarization, see **Figure 2**d. Apart from the cavity mode, the second resonance under TM polarization is a spoof surface plasmon (SP) whose wavelength is determined by the grating period. The existence of surface plasmon polaritons at the interface between the top gold layer and the nanocrystal film can be derived from Maxwell's equations for TM polarization. [46] In the absence of the grating, the surface plasmon polariton cannot be optically excited by free-space photons due to momentum mismatch. However, in our structure, diffracted light from the grating stripes acquires extra momentum and thus can couple with the surface plasmon polaritons. As a result, the period can be set at 1800 nm to match the SP with the exciton and broaden the band edge feature of the NCs, although other values have also been explored, see **Figure 2**b. In this case, we generate the SP resonance at 3.9 µm (**Figure 2**e), and the photocurrent spectrum presents a strong peak corresponding to the cavity and plasmon-enhanced band edge. When shorter periods are chosen, the SP resonance occurs at shorter wavelengths, and the cavity mode becomes visible at the band edge, leading to two observable features. More detailed information on the design procedure is given in Figure S5 and S8-S12.

Under TE polarization, the effective optical index discontinuity between the HgTe on sapphire and the HgTe NC film on top of the metal allows for reflection to occur, forming a Fabry Perot cavity with resonance wavelength determined by the distance between the stripes. This resonance does not match the band edge and appears blue-shifted, see **Figure 2**c and f, but contributes to the broadening and enhancing of the absorption signal.

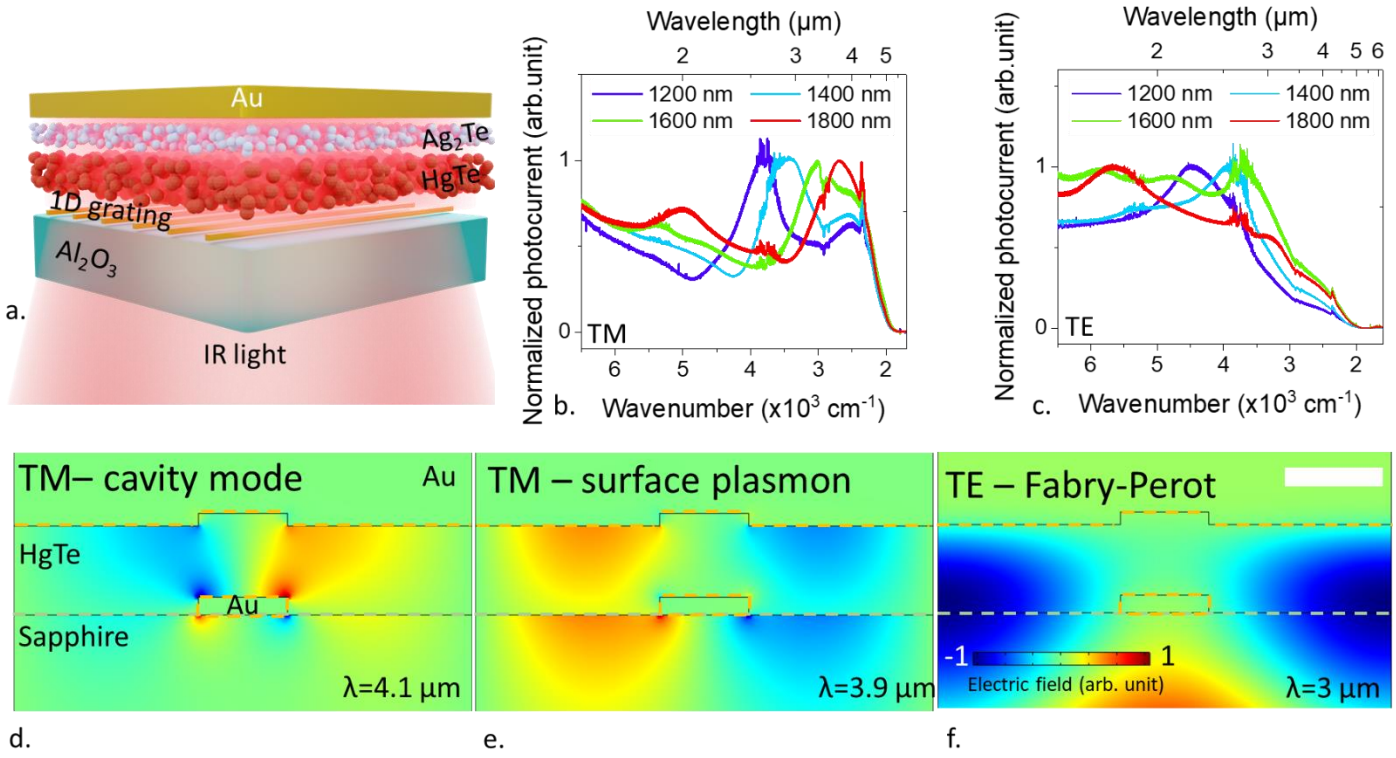

Figure 2 Resonant 1D grating used as a transparent conductive electrode. *a. Schematic of a photodiode based on sapphire/1D Au grating/HgTe/Ag_2Te/Au stack. b. (resp c.) Photocurrent spectra for the diode depicted in a. for various values of the grating period in TM (resp TE) polarization. Broad features at 5370, 3830 and 2890 cm^{-1} are due to water absorption, while the CO_2 is leading to a sharp feature at 2350 cm^{-1}. d. Absorption map in TM polarization at 4.1 μm. e. Absorption map in TM polarization at 3.9 μm. f. Absorption map in TE polarization at 3 μm. Parts d-f have been performed while the grating period is 1800 nm, the gold stripe width is 350 nm, and the NC film thickness is 350 nm. The common scale bar for parts d -f is 400 nm.*

Regarding the diode stack thickness, hopping transport in NC films limits the carrier mobilities in HgTe and thus a thick NC film ($\geq 500\,nm$) is not favorable for the photocurrent collection. On the other hand, too thin NC film could result in poor light absorption and increased ohmic losses in the metal. We thus optimize the diode stack thickness to maximize the overall NC device absorption, considering that a reasonable film thickness for efficient charge transport is usually below 500 nm, see Figure S11-12. The basic design guideline for ITO-based diodes is: the thicker the diode, the better. On the contrary, we identify an optimum thickness for the absorbing layer coupled to the grating corresponding to 350 nm. It is worth mentioning that the choice of the top gold layer thickness is also important. Usually, such metallic back reflector thickness is generally designed to match the material skin depth. Here, we have observed that a top metallic layer with a thickness below 80 nm can be optically leaky and therefore reduce the absorption within the NC layer.

Application to mid-infrared sensing

Now that the concept of the metallic grating is established, we switch to a 2D grid with a square lattice to maximize the resonance absorption in both polarizations, see **Figure 3**a. Note that, far from the resonance, the overall transmission of the grid is reduced with respect to that of the grating, as the structure is equivalent to two crossed polarizers. The benefit of such a 2D grid over the 1D grating and the ITO layer is depicted in **Figure 3**b-d: the absorption is selectively increased close to the exciton peak, while it is reduced at shorter wavelengths, resulting in an increased responsivity We observe on the photocurrent spectra (**Figure 3**b) a dramatically enhanced signal over the MWIR

region thanks to the designed resonances, while the rectifying behaviour is mostly maintained, see Figure S13-15. When comparing the grid to the ITO device, we can see that the photocurrent signal is also increased away from the resonances thanks to the improved transmission and reduced contact resistance.

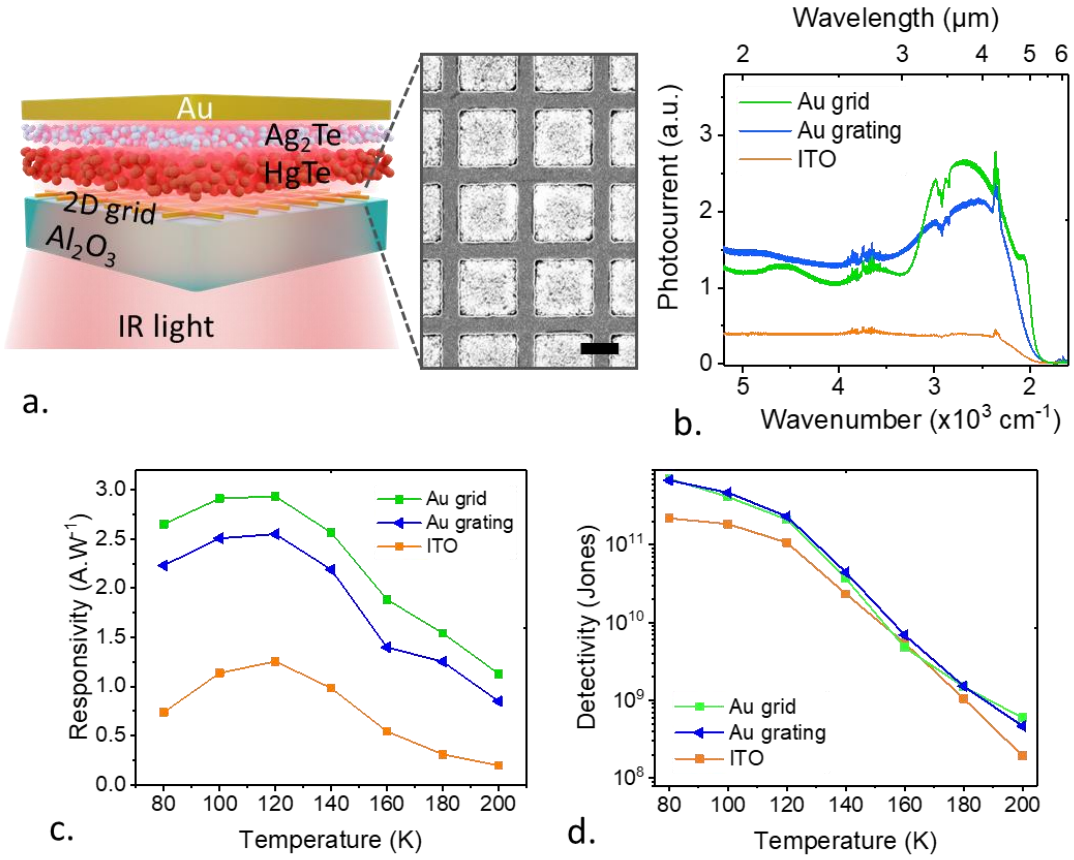

Figure 3 Resonant 2D grid for mid-wave photodiodes. *a. Schematic of a photodiode based on sapphire/2D Au grid/HgTe/Ag_2Te/Au stack. On the right panel, we show an SEM image of a fabricated 2D gold grid. The scale bar is 1 μm. b. Photocurrent spectra for a diode in which the bottom electrode is made of ITO film, 1D grating, and 2D grid. For both grating and grid electrodes, the Au stripe width and periodicity are s = 350 nm and p = 1800 nm, respectively. c. Responsivity (in front of a 600°C blackbody source) as a function of the temperature for a diode in which the bottom electrode is made of ITO film, 1D grating, and 2D grid. d. Specific detectivity (at 1 kHz) as a function of the temperature for a diode in which the bottom electrode is made of ITO film, 1D grating, and 2D grid.*

Responsivity is very close to 3 $A.W^{-1}$, whereas a 100 % external efficiency would correspond to 3.2 $A.W^{-1}$ for a device with a 4 μm peak. Note that the polarization independence introduced by the grid should have increased the responsivity by a factor of two. However, one should take into account the increased reflectivity of the device and metal losses due to the higher filling factor of the 2D grid. On the one hand, the reflection for out-of-resonance wavelengths increases due to higher metal coverage. On the other hand, NC absorption resulting from the surface plasmon resonance in 2D grid is not exactly double of that of the 1D grating because the additional metal stripes limit the spatial overlap of the mode with the NCs. At cryogenic temperature, white noise is prevailing, see Figure S13. The specific detectivity at 80 K is $7x10^{11}$ jones, while the device presents a 5 μm cut-off wavelength. This is currently the highest value reported for a mid-wave infrared photodiode based

on NCs, see Table 1 for detection figures of merit of state-of-the-art mid-wave infrared-operated NC-based devices.

The device's time response ($T_{90-10\%}$) to a pulse of light from a quantum cascade laser resonant with the particle band edge is around 80 ns (Figure S15) for a device size of 100x100 µm^2, close to the laser rise time. Thus, we also have used a complementary approach to determine the device bandwidth by applying a microwave rectification technique (*i.e.,* only dark current). In this case, the -3 dB bandwidth is found to be around 20 MHz, corresponding to a rise time of $t_{rise}=0.35/f_{3dB}\approx18$ ns. This suggests that the device's dynamics are mainly determined by the capacitance of the diode.

*Table 1 Figures of merit relative to light sensors operating in the MWIR and based on NCs. (PC: photoconductive, PT: phototransistor, PD: photodiode, * set-up limited)*

Absorbing material/Cut-off λ (µm)	**Operating mode**	**Responsivity** (A.W^{-1})	**Response time**	**Detectivity** (jones)	**Operating temperature** (K)	**Specific feature**	**Ref.**
Intraband MWIR device							
HgSe	PC	5 x 10^{-4}		8.5 x 10^8	80	intraband	[47]
HgSe	PC	0.7	8.75 ms	10^8	300	intraband	[48]
HgSe	PD	5 x 10^{-3}	200 ns	2 x 10^9	80	Intraband/mixed materials	[12]
HgSe	PC	77 x 10^{-3}	1 µs	1.7 x 10^9	80	intraband	[49]
HgSe	PC	0.145	2.1 s	-	300	intraband	[50]
Ag$_2$Se	PD	19 x 10^{-3}	-	7.8 x 10^6	300	intraband barrier device	[51]
Ag$_2$Se	PC	13.3 x 10^{-3}	-	3 x 10^5	300	intraband barrier device	[52]
Ag$_2$Se	PC	8 x 10^{-6}	~10s	-	300	intraband	[53]
Ag$_2$Se	PC	350 x 10^{-6}	-	-	90	intraband	[54]
Inter band MWIR device							
HgTe	PC	0.25	-	2 x 10^9	130	Agregated material	[55]
HgTe	PD	1.3	1 µs	3.3 x 10^{11}	85	Fisrt diode with Ag$_2$Te as HTL	[37]
HgTe	PD	1.62	-	4 x 10^{11}	85	With resonator	[18]
HgTe	PD	0.4	2.5 µs*	3 x 10^{10}	85	Stack diode	[33]

HgTe	PD	2.7	-	2.7 x 10^{11}	80	Homo p-i-n junction	[10]
HgTe	PC	0.7	11 µs*	2 x 10^{10}	80	Multiresonant pattern	[30]
HgTe	PD	2.65	80 ns	7 x 10^{11}	80		**This work**

In the first part of the paper, we demonstrated that metallic grids and gratings could advantageously replace TCO. In the last part of the paper, we show that the resonant electrode opens up a new degree of freedom and can be used to obtain novel functions, such as a bias-reconfigurable response. For this purpose, multiple gratings with different periods have been fabricated on the same chip. As mentioned, the grating period determines the diode spectral response, as shown in **Figure 2**b and c. Now, instead of operating the diodes in a solely vertical geometry, we apply bias between two electrodes, each connected to a grating, see **Figure 4**a. This method enables the formation of back-to-back diodes from a single diode stack (see **Figure 4**b), which considerably eases the fabrication compared to the approach where multiple diodes are built on top of each other.[33,36,56]

Here, by only using HgTe NCs with a 5 µm cut-off wavelength and properly coupling two gratings of similar polarization, it is possible to obtain a bias switch of the response from MWIR to SWIR only, see **Figure 4**c and Figure S16. Under 0 V operation, current sign is directly connected to the spectral range where the grating presents a resonance, enabling the use of photocurrent sign as spectral information, see Figure S16b.

This approach also enables generating new strategies to reshape the spectral response. When the currents flowing in the two diodes are equal in intensity, since they are opposite in sign, the device's overall response becomes null. This effect leads to a spectral band rejection. In **Figure 4**d, we show that the spectral response at 3 µm can be turned off while MWIR band remains strong (the green part). This property can be particularly interesting to prevent optical countermeasures. Indeed, a typical countermeasure strategy to prevent infrared imaging is blurring the sensor using a high-power laser. In our device, thanks to the capacity to turn off the response over a selected band, possible saturation of the detector can be prevented, such that it is possible to continue imaging even if the detector has been spotted.

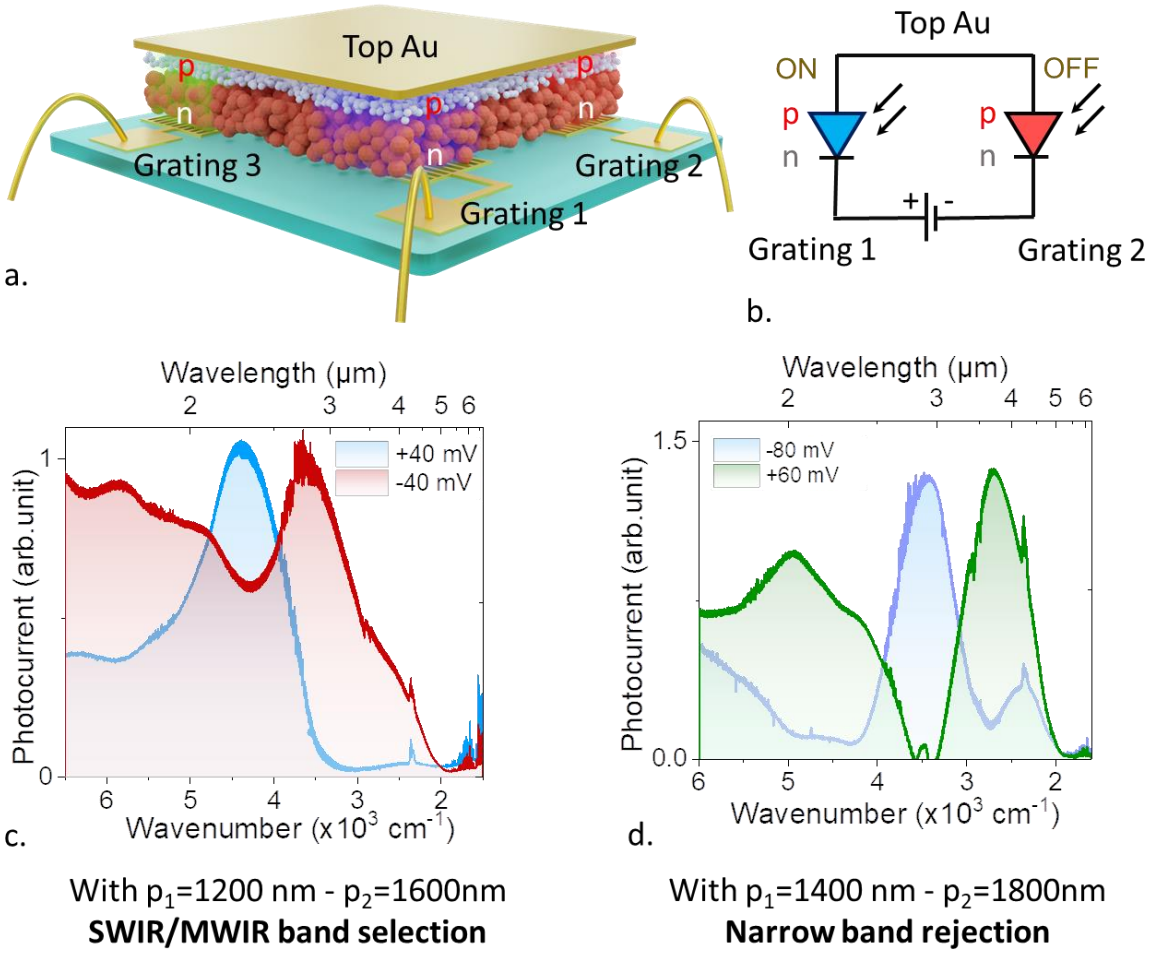

Figure 4 Band filtering properties of back-to-back diodes. *a. Schematic of an array of back-to-back diodes in which the periods of the two bottom electrodes are varied. In vertical diode configuration, the grating period determines the resonance wavelength for each diode. A back-to-back diode configuration can be created by applying a bias voltage through the bottom gratings. b. Equivalent circuit for the back-to-back diode. Depending on the bias sign, the diode is either connected in forward or reverse mode. In this example, only the diode associated with grating 1 is activated. c. Photocurrent (absolute value) spectra under +/- 40 mV in the case where 1200 and 1600 nm gratings are selected. With bias, the MWIR response can be turned ON and OFF. d. Photocurrent (absolute value) spectra, under positive and negative bias, in the case where 1400 and 1800 nm gratings are selected. With bias, the response of a narrow band can be turned ON and OFF.*

To summarize, the concept of transparent conductive electrodes for infrared offers no straightforward strategy. Here, we demonstrate that a careful design of metallic grating can minimize the optical loss while enhancing the effective absorption in the active semiconductor layer. Here, we propose a strategy combining three resonances from a single grating. The obtained device presents outstanding performances with responsivity close to 3 $A.W^{-1}$ corresponding to EQE above 90% for a device with 5 µm cut-off wavelength and operation at 80 K. Detectivity at cryogenic temperature reaches $7x10^{11}$ jones, while the diode response time under mid-wave infrared excitation is below 100 ns. We also demonstrate that different metallic gratings can be combined with a single diode stack to form multicolor and reconfigurable photodiodes. Compared to existing strategies, our approach is far easier to fabricate while offering new functionalities, such as band rejection, which can be used against countermeasure applications. Now that MWIR NC-based sensors achieve high performances, it becomes clear that the next challenge will be raising the operating temperature to reach hot operation[10,57] (*i.e.,* above 130 K).

DATA AVAILABILITY

The data that support the findings of this study are available from the corresponding author upon request.

REFERENCES

(1) Hafiz, S. B.; Scimeca, M.; Sahu, A.; Ko, D.-K. Colloidal Quantum Dots for Thermal Infrared Sensing and Imaging. *Nano Converg.* **2019**, *6*, 7. https://doi.org/10.1186/s40580-019-0178-1.

(2) V. Pejović; E. Georgitzikis; J. Lee; I. Lieberman; D. Cheyns; P. Heremans; P. E. Malinowski. Infrared Colloidal Quantum Dot Image Sensors. *IEEE Trans. Electron Devices* **2022**, *69*, 2840–2850. https://doi.org/10.1109/TED.2021.3133191.

(3) Maniyara, R. A.; Graham, C.; Paulillo, B.; Bi, Y.; Chen, Y.; Herranz, G.; Baker, D. E.; Mazumder, P.; Konstantatos, G.; Pruneri, V. Highly Transparent and Conductive ITO Substrates for near Infrared Applications. *APL Mater.* **2021**, *9*, 021121. https://doi.org/10.1063/5.0040864.

(4) Shen, X.; Peterson, J. C.; Guyot-Sionnest, P. Mid-Infrared HgTe Colloidal Quantum Dot LEDs. *ACS Nano* **2022**, *16*, 7301–7308. https://doi.org/10.1021/acsnano.2c01694.

(5) Qu, J.; Rastogi, P.; Gréboval, C.; Lagarde, D.; Chu, A.; Dabard, C.; Khalili, A.; Cruguel, H.; Robert, C.; Xu, X. Z.; Ithurria, S.; Silly, M. G.; Ferré, S.; Marie, X.; Lhuillier, E. Electroluminescence from HgTe Nanocrystals and Its Use for Active Imaging. *Nano Lett.* **2020**, *20*, 6185–6190. https://doi.org/10.1021/acs.nanolett.0c02557.

(6) Gréboval, C.; Chu, A.; Goubet, N.; Livache, C.; Ithurria, S.; Lhuillier, E. Mercury Chalcogenide Quantum Dots: Material Perspective for Device Integration. *Chem. Rev.* **2021**, *121*, 3627–3700. https://doi.org/10.1021/acs.chemrev.0c01120.

(7) Zhao, X.; Mu, G.; Tang, X.; Chen, M. Mid-IR Intraband Photodetectors with Colloidal Quantum Dots. *Coatings* **2022**, *12*, 467. https://doi.org/10.3390/coatings12040467.

(8) Nakotte, T.; Munyan, S. G.; Murphy, J. W.; Hawks, S. A.; Kang, S.; Han, J.; Hiszpanski, A. M. Colloidal Quantum Dot Based Infrared Detectors: Extending to the Mid-Infrared and Moving from the Lab to the Field. *J. Mater. Chem. C* **2022**, *10*, 790–804. https://doi.org/10.1039/D1TC05359K.

(9) Yang, J.; Lv, Y.; He, Z.; Wang, B.; Chen, S.; Xiao, F.; Hu, H.; Yu, M.; Liu, H.; Lan, X.; Hsu, H.-Y.; Song, H.; Tang, J. Bi2S3 Electron Transport Layer Incorporation for High-Performance Heterostructure HgTe Colloidal Quantum Dot Infrared Photodetectors. *ACS Photonics* **2023**, *10*, 2226–2233. https://doi.org/10.1021/acsphotonics.2c01145.

(10) Xue, X.; Chen, M.; Luo, Y.; Qin, T.; Tang, X.; Hao, Q. High-Operating-Temperature Mid-Infrared Photodetectors via Quantum Dot Gradient Homojunction. *Light Sci. Appl.* **2023**, *12*, 2. https://doi.org/10.1038/s41377-022-01014-0.

(11) Georgitzikis, E.; Malinowski, P. E.; Maes, J.; Hadipour, A.; Hens, Z.; Heremans, P.; Cheyns, D. Optimization of Charge Carrier Extraction in Colloidal Quantum Dots Short-Wave Infrared Photodiodes through Optical Engineering. *Adv. Funct. Mater.* **2018**, *28*, 1804502. https://doi.org/10.1002/adfm.201804502.

(12) Livache, C.; Martinez, B.; Goubet, N.; Gréboval, C.; Qu, J.; Chu, A.; Royer, S.; Ithurria, S.; Silly, M. G.; Dubertret, B.; Lhuillier, E. A Colloidal Quantum Dot Infrared Photodetector and Its Use for Intraband Detection. *Nat. Commun.* **2019**, *10*, 2125. https://doi.org/10.1038/s41467-019-10170-8.

(13) Galagan, Y.; Zimmermann, B.; Coenen, E. W. C.; Jørgensen, M.; Tanenbaum, D. M.; Krebs, F. C.; Gorter, H.; Sabik, S.; Slooff, L. H.; Veenstra, S. C.; Kroon, J. M.; Andriessen, R. Current Collecting Grids for ITO-Free Solar Cells. *Adv. Energy Mater.* **2012**, *2*, 103–110. https://doi.org/10.1002/aenm.201100552.

(14) Lim, J. W.; Lee, Y. T.; Pandey, R.; Yoo, T.-H.; Sang, B.-I.; Ju, B.-K.; Hwang, D. K.; Choi, W. K. Effect of Geometric Lattice Design on Optical/Electrical Properties of Transparent Silver Grid for Organic Solar Cells. *Opt. Express* **2014**, *22*, 26891–26899. https://doi.org/10.1364/OE.22.026891.
(15) Choi, Y.; Kim, D.; Do, E. C.; Kim, D.; Mun, J.; Lee, J. W.; Lee, Y.; Kim, Y. G. Interdigitated Front Contact Crystalline Silicon Solar Cell. *Sol. Energy* **2014**, *100*, 94–101. https://doi.org/10.1016/j.solener.2013.12.007.
(16) Gupta, D. K.; Langelaar, M.; Barink, M.; van Keulen, F. Optimizing Front Metallization Patterns: Efficiency with Aesthetics in Free-Form Solar Cells. *Renew. Energy* **2016**, *86*, 1332–1339. https://doi.org/10.1016/j.renene.2015.09.071.
(17) Le-Van, Q.; Le Roux, X.; Aassime, A.; Degiron, A. Electrically Driven Optical Metamaterials. *Nat. Commun.* **2016**, *7*, 12017. https://doi.org/10.1038/ncomms12017.
(18) Tang, X.; Ackerman, M. M.; Guyot-Sionnest, P. Thermal Imaging with Plasmon Resonance Enhanced HgTe Colloidal Quantum Dot Photovoltaic Devices. *ACS Nano* **2018**, *12*, 7362–7370. https://doi.org/10.1021/acsnano.8b03871.
(19) Rastogi, P.; Chu, A.; Dang, T. H.; Prado, Y.; Gréboval, C.; Qu, J.; Dabard, C.; Khalili, A.; Dandeu, E.; Fix, B.; Xu, X. Z.; Ithurria, S.; Vincent, G.; Gallas, B.; Lhuillier, E. Complex Optical Index of HgTe Nanocrystal Infrared Thin Films and Its Use for Short Wave Infrared Photodiode Design. *Adv. Opt. Mater.* **2021**, *9*, 2002066. https://doi.org/10.1002/adom.202002066.
(20) Lezec, H. J.; Degiron, A.; Devaux, E.; Linke, R. A.; Martin-Moreno, L.; Garcia-Vidal, F. J.; Ebbesen, T. W. Beaming Light from a Subwavelength Aperture. *Science* **2002**, *297*, 820–822. https://doi.org/10.1126/science.1071895.
(21) Liu, H.; Lalanne, P. Microscopic Theory of the Extraordinary Optical Transmission. *Nature* **2008**, *452*, 728–731. https://doi.org/10.1038/nature06762.
(22) S. G. Rodrigo; F. de León-Pérez; L. Martín-Moreno. Extraordinary Optical Transmission: Fundamentals and Applications. *Proc. IEEE* **2016**, *104*, 2288–2306. https://doi.org/10.1109/JPROC.2016.2580664.
(23) Gordon, R.; Sinton, D.; Kavanagh, K. L.; Brolo, A. G. A New Generation of Sensors Based on Extraordinary Optical Transmission. *Acc. Chem. Res.* **2008**, *41*, 1049–1057. https://doi.org/10.1021/ar800074d.
(24) Vala, M.; Ertsgaard, C. T.; Wittenberg, N. J.; Oh, S.-H. Plasmonic Sensing on Symmetric Nanohole Arrays Supporting High-Q Hybrid Modes and Reflection Geometry. *ACS Sens.* **2019**, *4* , 3265–3274. https://doi.org/10.1021/acssensors.9b01780.
(25) Gopalan, K. K.; Paulillo, B.; Mackenzie, D. M. A.; Rodrigo, D.; Bareza, N.; Whelan, P. R.; Shivayogimath, A.; Pruneri, V. Scalable and Tunable Periodic Graphene Nanohole Arrays for Mid-Infrared Plasmonics. *Nano Lett.* **2018**, *18*, 5913–5918. https://doi.org/10.1021/acs.nanolett.8b02613.
(26) Tong, J.; Suo, F.; Ma, J.; Tobing, L. Y. M.; Qian, L.; Zhang, D. H. Surface Plasmon Enhanced Infrared Photodetection. *Opto-Electron. Adv.* **2018**, *2*, 180026–1. https://doi.org/10.29026/oea.2019.180026.
(27) Yan, N.; Qiu, Y.; He, X.; Tang, X.; Hao, Q.; Chen, M. Plasmonic Enhanced Nanocrystal Infrared Photodetectors. *Materials* **2023**, *16*. https://doi.org/10.3390/ma16083216.
(28) Chen, M.; Lu, L.; Yu, H.; Li, C.; Zhao, N. Integration of Colloidal Quantum Dots with Photonic Structures for Optoelectronic and Optical Devices. *Adv. Sci.* **2021**, *8*, 2101560. https://doi.org/10.1002/advs.202101560.
(29) Dang, T. H.; Khalili, A.; Abadie, C.; Gréboval, C.; Cavallo, M.; Zhang, H.; Bossavit, E.; Utterback, J. K.; Dandeu, E.; Prado, Y.; Vincent, G.; Ithurria, S.; Todorov, Y.; Sirtori, C.; Vasanelli, A.; Lhuillier, E. Nanocrystal-Based Active Photonics Device through Spatial Design of Light-Matter Coupling. *ACS Photonics* **2022**, *9*, 2528–2535. https://doi.org/10.1021/acsphotonics.2c00738.
(30) Dang, T. H.; Abadie, C.; Khalili, A.; Gréboval, C.; Zhang, H.; Prado, Y.; Xu, X. Z.; Gacemi, D.; Descamps-Mandine, A.; Ithurria, S.; Todorov, Y.; Sirtori, C.; Vasanelli, A.; Lhuillier, E.

Broadband Enhancement of Mid-Wave Infrared Absorption in a Multi-Resonant Nanocrystal-Based Device. *Adv. Opt. Mater.* **2022**, *10*, 2200297. https://doi.org/10.1002/adom.202200297.
(31) Dang, T. H.; Vasanelli, A.; Todorov, Y.; Sirtori, C.; Prado, Y.; Chu, A.; Gréboval, C.; Khalili, A.; Cruguel, H.; Delerue, C.; Vincent, G.; Lhuillier, E. Bias Tunable Spectral Response of Nanocrystal Array in a Plasmonic Cavity. *Nano Lett.* **2021**, *21*, 6671–6677. https://doi.org/10.1021/acs.nanolett.1c02193.
(32) Lhuillier, E.; Robin, A.; Ithurria, S.; Aubin, H.; Dubertret, B. Electrolyte-Gated Colloidal Nanoplatelets-Based Phototransistor and Its Use for Bicolor Detection. *Nano Lett.* **2014**, *14*, 2715–2719. https://doi.org/10.1021/nl5006383.
(33) Tang, X.; Ackerman, M. M.; Chen, M.; Guyot-Sionnest, P. Dual-Band Infrared Imaging Using Stacked Colloidal Quantum Dot Photodiodes. *Nat. Photonics* **2019**, *13*, 277–282. https://doi.org/10.1038/s41566-019-0362-1.
(34) Tang, X.; Tang, X.; Lai, K. W. C. Scalable Fabrication of Infrared Detectors with Multispectral Photoresponse Based on Patterned Colloidal Quantum Dot Films. *ACS Photonics* **2016**, *3*, 2396–2404. https://doi.org/10.1021/acsphotonics.6b00620.
(35) Tang, X.; Ackerman, M. M.; Guyot-Sionnest, P. Acquisition of Hyperspectral Data with Colloidal Quantum Dots. *Laser Photonics Rev.* **2019**, *13*, 1900165. https://doi.org/10.1002/lpor.201900165.
(36) Zhang, S.; Mu, G.; Cao, J.; Luo, Y.; Hao, Q.; Chen, M.; Tan, Y.; Zhao, P.; Tang, X. Single-/Fused-Band Dual-Mode Mid-Infrared Imaging with Colloidal Quantum-Dot Triple-Junctions. *Photonics Res.* **2022**, *10*, 1987–1995. https://doi.org/10.1364/PRJ.458351.
(37) Ackerman, M. M.; Tang, X.; Guyot-Sionnest, P. Fast and Sensitive Colloidal Quantum Dot Mid-Wave Infrared Photodetectors. *ACS Nano* **2018**, *12*, 7264–7271. https://doi.org/10.1021/acsnano.8b03425.
(38) Keuleyan, S.; Lhuillier, E.; Guyot-Sionnest, P. Synthesis of Colloidal HgTe Quantum Dots for Narrow Mid-IR Emission and Detection. *J. Am. Chem. Soc.* **2011**, *133*, 16422–16424. https://doi.org/10.1021/ja2079509.
(39) Martinez, B.; Ramade, J.; Livache, C.; Goubet, N.; Chu, A.; Gréboval, C.; Qu, J.; Watkins, W. L.; Becerra, L.; Dandeu, E.; Fave, J. L.; Méthivier, C.; Lacaze, E.; Lhuillier, E. HgTe Nanocrystal Inks for Extended Short-Wave Infrared Detection. *Adv. Opt. Mater.* **2019**, *7*, 1900348. https://doi.org/10.1002/adom.201900348.
(40) Lan, X.; Chen, M.; Hudson, M. H.; Kamysbayev, V.; Wang, Y.; Guyot-Sionnest, P.; Talapin, D. V. Quantum Dot Solids Showing State-Resolved Band-like Transport. *Nat. Mater.* **2020**, *19*, 323–329. https://doi.org/10.1038/s41563-019-0582-2.
(41) Bossavit, E.; Qu, J.; Abadie, C.; Dabard, C.; Dang, T.; Izquierdo, E.; Khalili, A.; Gréboval, C.; Chu, A.; Pierini, S.; Cavallo, M.; Prado, Y.; Parahyba, V.; Xu, X. Z.; Decamps-Mandine, A.; Silly, M.; Ithurria, S.; Lhuillier, E. Optimized Infrared LED and Its Use in an All-HgTe Nanocrystal-Based Active Imaging Setup. *Adv. Opt. Mater.* **2022**, *10*, 2101755. https://doi.org/10.1002/adom.202101755.
(42) Ackerman, M. M.; Chen, M.; Guyot-Sionnest, P. HgTe Colloidal Quantum Dot Photodiodes for Extended Short-Wave Infrared Detection. *Appl. Phys. Lett.* **2020**, *116*, 083502. https://doi.org/10.1063/1.5143252.
(43) Rastogi, P.; Izquierdo, E.; Gréboval, C.; Cavallo, M.; Chu, A.; Dang, T. H.; Khalili, A.; Abadie, C.; Alchaar, R.; Pierini, S.; Cruguel, H.; Witkowski, N.; Utterback, J. K.; Brule, T.; Xu, X. Z.; Hollander, P.; Ouerghi, A.; Gallas, B.; Silly, M. G.; Lhuillier, E. Extended Short-Wave Photodiode Based on CdSe/HgTe/Ag2Te Stack with High Internal Efficiency. *J. Phys. Chem. C* **2022**, *126*, 13720–13728. https://doi.org/10.1021/acs.jpcc.2c02044.
(44) Gréboval, C.; Izquierdo, E.; Abadie, C.; Khalili, A.; Cavallo, M.; Chu, A.; Dang, T. H.; Zhang, H.; Lafosse, X.; Rosticher, M.; Xu, X. Z.; Descamps-Mandine, A.; Ouerghi, A.; Silly, M. G.; Ithurria, S.; Lhuillier, E. HgTe Nanocrystal-Based Photodiode for Extended Short-Wave Infrared Sensing with Optimized Electron Extraction and Injection. *ACS Appl. Nano Mater.* **2022**, *5*, 8602–8611. https://doi.org/10.1021/acsanm.2c02103.

(45) Todorov, Y.; Tosetto, L.; Teissier, J.; Andrews, A. M.; Klang, P.; Colombelli, R.; Sagnes, I.; Strasser, G.; Sirtori, C. Optical Properties of Metal-Dielectric-Metal Microcavities in the THz Frequency Range. *Opt. Express* **2010**, *18*, 13886–13907. https://doi.org/10.1364/OE.18.013886.
(46) Maier, S. A. Surface Plasmon Polaritons at Metal / Insulator Interfaces. In *Plasmonics: Fundamentals and Applications*; Maier, S. A., Ed.; Springer US: New York, NY, 2007; pp 21–37. https://doi.org/10.1007/0-387-37825-1_2.
(47) Deng, Z.; Jeong, K. S.; Guyot-Sionnest, P. Colloidal Quantum Dots Intraband Photodetectors. *ACS Nano* **2014**, *8*, 11707–11714. https://doi.org/10.1021/nn505092a.
(48) Lhuillier, E.; Scarafagio, M.; Hease, P.; Nadal, B.; Aubin, H.; Xu, X. Z.; Lequeux, N.; Patriarche, G.; Ithurria, S.; Dubertret, B. Infrared Photodetection Based on Colloidal Quantum-Dot Films with High Mobility and Optical Absorption up to THz. *Nano Lett.* **2016**, *16*, 1282–1286. https://doi.org/10.1021/acs.nanolett.5b04616.
(49) Chen, M.; Hao, Q.; Luo, Y.; Tang, X. Mid-Infrared Intraband Photodetector via High Carrier Mobility HgSe Colloidal Quantum Dots. *ACS Nano* **2022**, *16*, 11027–11035. https://doi.org/10.1021/acsnano.2c03631.
(50) Tang, X.; Wu, G. fu; Lai, K. W. C. Plasmon Resonance Enhanced Colloidal HgSe Quantum Dot Filterless Narrowband Photodetectors for Mid-Wave Infrared. *J. Mater. Chem. C* **2017**, *5*, 362–369. https://doi.org/10.1039/C6TC04248A.
(51) Hafiz, S. B.; Al Mahfuz, M. M.; Lee, S.; Ko, D.-K. Midwavelength Infrared p–n Heterojunction Diodes Based on Intraband Colloidal Quantum Dots. *ACS Appl. Mater. Interfaces* **2021**, *13*, 49043–49049. https://doi.org/10.1021/acsami.1c14749.
(52) Hafiz, S. B.; Al Mahfuz, M. M.; Ko, D.-K. Vertically Stacked Intraband Quantum Dot Devices for Mid-Wavelength Infrared Photodetection. *ACS Appl. Mater. Interfaces* **2021**, *13*, 937–943. https://doi.org/10.1021/acsami.0c19450.
(53) Qu, J.; Goubet, N.; Livache, C.; Martinez, B.; Amelot, D.; Gréboval, C.; Chu, A.; Ramade, J.; Cruguel, H.; Ithurria, S.; Silly, M. G.; Lhuillier, E. Intraband Mid-Infrared Transitions in Ag2Se Nanocrystals: Potential and Limitations for Hg-Free Low-Cost Photodetection. *J. Phys. Chem. C* **2018**, *122*, 18161–18167. https://doi.org/10.1021/acs.jpcc.8b05699.
(54) Hafiz, S. B.; Scimeca, M. R.; Zhao, P.; Paredes, I. J.; Sahu, A.; Ko, D.-K. Silver Selenide Colloidal Quantum Dots for Mid-Wavelength Infrared Photodetection. *ACS Appl. Nano Mater.* **2019**, *2*, 1631–1636. https://doi.org/10.1021/acsanm.9b00069.
(55) Keuleyan, S.; Lhuillier, E.; Brajuskovic, V.; Guyot-Sionnest, P. Mid-Infrared HgTe Colloidal Quantum Dot Photodetectors. *Nat. Photonics* **2011**, *5*, 489–493. https://doi.org/10.1038/nphoton.2011.142.
(56) Wang, S.; Ashokan, A.; Balendhran, S.; Yan, W.; Johnson, B. C.; Peruzzo, A.; Crozier, K. B.; Mulvaney, P.; Bullock, J. Room Temperature Bias-Selectable, Dual-Band Infrared Detectors Based on Lead Sulfide Colloidal Quantum Dots and Black Phosphorus. *ACS Nano* **2023**, 17, 11771–11782. https://doi.org/10.1021/acsnano.3c02617.
(57) Peterson, J. C.; Guyot-Sionnest, P. Room-Temperature 15% Efficient Mid-Infrared HgTe Colloidal Quantum Dot Photodiodes. *ACS Appl. Mater. Interfaces* **2023**, *15*, 19163–19169. https://doi.org/10.1021/acsami.3c00487.

ACKNOWLEDEGMENTS

The project is supported by ERC starting grant blackQD (grant n° 756225) and AQDtive (grant n°101086358). We acknowledge the use of clean-room facilities from the “Centrale de Proximité Paris-Centre” and the french RENATECH network. This work was supported by French state funds managed by the ANR more specifically within the grants Copin (ANR-19-CE24-0022), Frontal (ANR-19-CE09-0017), Graskop (ANR-19-CE09-0026), NITQuantum (ANR-20-ASTR-0008-01), Bright (ANR-21-CE24-0012-02), MixDferro (ANR-21-CE09-0029) and Quicktera (ANR-22-CE09-0018).

Author contributions

A.V. and E.L. designed the project and made it funded. Y.P. and A.K. synthesized the nanoparticles under the supervision of S.I. T.H.D., A.V., and G.V. with support of Y.T. and C.S. performed the electromagnetic simulation. T.H.D. fabricated the device with clean room support of X.L., M.C., C.D., E.B., H.Z., N.L., and C.A. T.H.D. and D.G. conducted experimental characterization. T.H.D., A.V., and E.L. wrote the manuscript with input from all the authors. All authors have proofread the paper's content.

COMPETING INTEREST

The authors declare no competing interests.

Supporting Information

Supporting Information include (*i*) supplementary methods, (*ii*) HgTe NC used as infrared absorbing layer, (*iii*) Fabrication process of the diode, (*iv*) discussion of gold electrode motivation and resistance, (*v*) Performance of diode using ITO as transparent electrode, (*vi*) Electromagnetic design of the bottom electrode, (*vi*) Optimization of the diode geometrical factor, (*vii*) Performances of the diode with 2D multi resonant grid, (*viii*) Bias dependence of the back-to- back diode operation.

TOC Graphic

Metallic gratings for enhanced absorption and bias tunable photoresponse